Eur Biophys J (2010) 39:839–853
DOI 10.1007/s00249-009-0574-2

ORIGINAL PAPER

Structural modeling of calcium binding in the selectivity filter of the L-type calcium channel

Ricky C. K. Cheng · Denis B. Tikhonov · Boris S. Zhorov

Received: 19 August 2009 / Revised: 8 December 2009 / Accepted: 15 December 2009 / Published online: 7 January 2010

Abstract Calcium channels play crucial physiological roles. In the absence of high-resolution structures of the channels, the mechanism of ion permeation is unknown. Here we used a method proposed in an accompanying paper (Cheng and Zhorov in Eur Biophys J, 2009) to predict possible chelation patterns of calcium ions in a structural model of the L-type calcium channel. We compared three models in which two or three calcium ions interact with the four selectivity filter glutamates and a conserved aspartate adjacent to the glutamate in repeat II. Monte Carlo energy minimizations yielded many complexes with calcium ions bound to at least two selectivity filter carboxylates. In these complexes calcium-carboxylate attractions are counterbalanced by calcium-calcium and carboxylate-carboxylate repulsions. Superposition of the complexes suggests a high degree of mobility of calcium ions and carboxylate groups of the glutamates. We used the predicted complexes to propose a permeation mechanism that involves single-file movement of calcium ions. The key feature of this mechanism is the presence of bridging glutamates that coordinate two calcium ions and enable their transitions between different chelating patterns involving four to six oxygen atoms from the channel protein. The conserved aspartate is proposed to coordinate a calcium ion incoming to the selectivity filter from the extracellular side. Glutamates in repeats III and IV, which are most distant from the repeat II aspartate, are proposed to coordinate the calcium ion that leaves the selectivity filter to the inner pore. Published experimental data and earlier proposed permeation models are discussed in view of our model.

Keywords Monte Carlo minimization · Ca^{2+} protein interactions · Homology modeling

Abbreviations

DEKA	The selectivity filter ring of Asp, Glu, Lys, and Ala residues from the four P-loop repeats of Na^+ channels
EEEE	The ring of glutamates in the selectivity filter of L-type Ca^{2+} channel
EEEED	Locus EEEE plus the Asp residue adjacent to the selectivity filter glutamate in repeat II
KvAP	A bacterial voltage-gated potassium channel
MC	Monte Carlo
MCM	Monte Carlo minimization
LTCC	L-type calcium channel

Introduction

Ca^{2+} channels play key roles in cell physiology (Hille 2001). Influx of Ca^{2+} ions in the cytosol via voltage-gated Ca^{2+} channels is coupled to cellular responses such as muscle contractions, hormone release, and gene expression (Catterall et al. 2005). The pore-forming α_1 subunit of Ca^{2+} channels contains four homologous repeats in a single-polypeptide chain. Each repeat includes six transmembrane α helices, S1-S6, and a membrane reentrant P-loop (P). The latter consists of the extracellular S5-P linker, a pore helix

R. C. K. Cheng · D. B. Tikhonov · B. S. Zhorov (✉)
Department of Biochemistry and Biomedical Sciences, McMaster University, Hamilton, ON, Canada
e-mail: zhorov@mcmaster.ca

D. B. Tikhonov
Sechenov Institute of Evolutionary Physiology and Biochemistry, Russian Academy of Sciences, St. Petersburg, Russia

(P-helix), an ascending limb that lines the outer pore, and the extracellular P-S6 linker. Four voltage-sensing domains are linked to the pore-forming domain composed of four S5-P-S6 sequences. X-ray structures of K^+ channels (Doyle et al. 1998; Jiang et al. 2002; Jiang et al. 2003; Long et al. 2005) show K^+ ions coordinated by the backbone oxygens from the four ascending limbs. In contrast, the selectivity filters in Na^+ and Ca^{2+} channels are formed by side chains of the highly conserved residues DEKA and EEEE, respectively, in homologous positions in the four ascending limbs. Ca^{2+} ions can bind to Ca^{2+} channels with high (μM) and low (mM) affinities (Sather and McCleskey 2003). The EEEE locus is involved in high-affinity binding of Ca^{2+} and block of monovalent currents by divalent cations (Sather and McCleskey 2003).

Models of the selectivity filter region of Ca^{2+} channels were proposed to predict measurable electrophysiological properties from such parameters as dimensions of the pore, dielectric permittivity, and concentration of cations and anions (Nonner et al. 2000; Corry et al. 2001; Boda et al. 2007, 2008; Gillespie and Boda 2008). These models do not provide structural details of the selectivity filter, which are important to understand experimental observations. For example, mutations of the selectivity filter glutamates in different repeats have unequal effects on ion permeation (Yang et al. 1993; Ellinor et al. 1995) and Ca^{2+} potentiation of drug binding (Dilmac et al. 2003, 2004). Ca^{2+}-dependent inactivation may involve structural rearrangement of the outer pore (Babich et al. 2007). Atomistic models are desirable to rationalize such observations.

In previous structural models, the selectivity filter glutamates were proposed to chelate Ca^{2+} ions in an asymmetric split (Zhorov and Ananthanarayanan 1996; Zhorov et al. 2001) and a symmetrical single-file (Lipkind and Fozzard 2001) fashion. These static models do not consider the flexibility of the selectivity filter glutamates and transient states in the permeation process. In this study, we employ a Ca^{2+} docking protocol proposed in the accompanying paper (Cheng and Zhorov 2009) to predict possible patterns of interaction of Ca^{2+} ions in the selectivity filter of the L-type calcium channel (LTCC). We use a homology model of the channel, in which dispositions of P-helices, selectivity filter residues, and the inner helices are inherited from previous models of sodium and calcium channels (Tikhonov and Zhorov 2005, 2008). Our calculations predicted multiple chelation patterns of Ca^{2+} ions. Analysis of these patterns allowed us to suggest a structural mechanism of Ca^{2+} permeation.

Methods

The $Ca_v1.2$ model comprises the P-loops region and the first 15 residues from each of the four inner helices (S6s). The X-ray structure of KvAP (Jiang et al. 2003) was used as a template for P-helices and S6 helices. Previous modeling with this template allowed us to propose mechanisms of action of benzothiazepines (Tikhonov and Zhorov 2008), dihydropyridines (Tikhonov and Zhorov 2009), and phenyalalkyamines (Cheng et al. 2009) in LTCC. The present study is focused on the selectivity filter region. Therefore, other segments of the pore domain, which are far from the selectivity filter and do not line the pore in X-ray structures of K^+ channels, are not included in the model (Fig. 1).

Ion selectivity and permeation in voltage-gated Ca^{2+} and Na^+ channels are controlled, respectively, by the EEEE and DEKA loci of residues that occupy matching positions in the P-loop sequences. Replacement of the DEKA locus with DEEE residues makes a Na^+ channel Ca^{2+}-selective (Heinemann et al. 1992), whereas replacement of the EEEE locus to EEKA residues makes a Ca^{2+} channel Na^+-selective (Tang et al. 1993). These experiments suggest a similar folding of the ascending limbs in voltage-gated Ca^{2+} and Na^+ channels. Based on these data, the ascending limbs of LTCC were folded as in our model of $Na_v1.4$ (Tikhonov and Zhorov 2005) using alignment shown in Table 1 (Zhorov et al. 2001). Repeats I to IV were arranged clockwise when viewed extracellularly (Dudley et al. 2000; Li et al. 2001). A universal scheme (Zhorov and Tikhonov 2004) is employed to label residues. A residue in the inner helix is labeled by the symbol "*i*" and a relative number starting from the N-terminus. A residue in the P-loop is labeled by the symbol "*p*" and a residue number relative to position *p50*, which corresponds to the DEKA locus in $Na_v1.4$, the EEEE locus in $Ca_v1.2$, and the valine in the TVGYG motif of KvAP. The selectivity filter glutamates (E^{p50}s) were ionized. D^{2p51} was ionized in some experiments. Other ionizable residues were kept neutral. This decreases uncertainty regarding protonation states and the presence of counterions, but is unlikely to have a significant impact on Ca^{2+} coordination by the selectivity filter residues.

Calculations were performed using the Monte Carlo-minimization protocol (Li and Scheraga 1987) in the ZMM program (http://www.zmmsoft.com). The energy was expressed as a sum of van der Waals, electrostatic, torsional, and hydration components. The AMBER force field (Weiner et al. 1984; Weiner et al. 1986) was used for nonbonded interactions. An implicit-solvent method was used (Lazaridis and Karplus 1999). Electrostatic interactions were calculated using the Coulomb law with the solvent exposure- and distance-dependent dielectric function $\varepsilon = d\,(4\text{–}3\,s)$, where d is the distance between interacting atoms, and s is a screening factor determined using a modified algorithm by Lazaridis and Karplus (1999). This screening factor ranges from *0* for a pair of water-exposed atoms to *1* for a pair of protein-buried atoms.

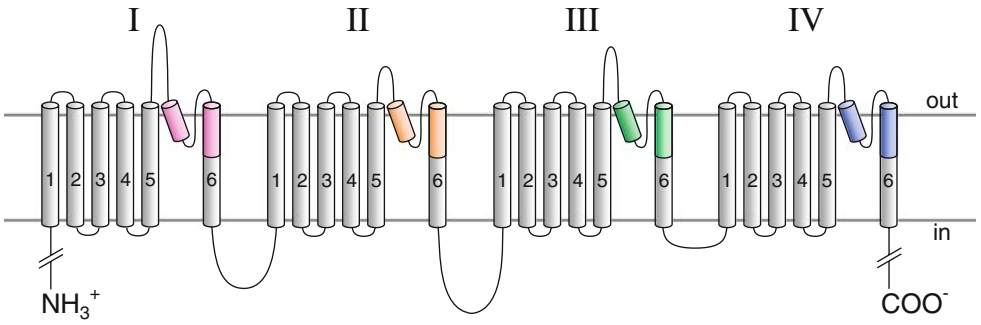


```
                        p36  p41       p51          i1        i11
                        |    |         |            |         |
                        ===P-helix===|^^^AL[a]^^     ======S6=======
KvAP                    VFDALWWAVVTATTVGYGDVVP       PIGKVIGIAVMLTGI
Cav1.2    I             FAFAMLTVFQCITMEGWTDVLY       ELPWVYFVSLVIFGS
         II             FPQSLLTVFQILTGEDWNSVMY       MLVCIYFIILFICGN
        III             VLAAMMALFTVSTFEGWPELLY       VEISIFFIIYIIIIA
         IV             FPQAVLLLFRCATGEAWQDIML       SFAVFYFISFYMLCA
Pins to KvAP            ++++++++++-----------        +++++++++++++
Pins to Nav1.4          ----------++++++++++        ---------------
[a] Ascending limbs
```

Fig. 1 Homology modeling of $Ca_v1.2$ outer pore. The α_1 subunit of the L-type calcium channel has four repeats, each repeat containing six transmembrane helices (S1–S6), and a P-loop between S5 and S6 helices. The segments included in the outer pore model presented in this study are *colored*. Alpha-carbons of the model were constrained to the respective atoms in either the KvAP X-ray structure (Jiang et al. 2003) or $Na_v1.4$ outer pore model (Tikhonov and Zhorov 2005) by pins. The "+" and "−" symbols below the sequence alignment denote, respectively, the presence and absence of pins that constrain the alpha-carbons of the model to corresponding templates. To maximize the flexibility of the selectivity filter during Ca^{2+} docking, no pins were applied to the selectivity filter glutamates and residues in adjacent positions

Table 1 Alignment of P-helices, ascending limbs, and inner helixes in P-loop channels

Channel	Segment	First residue[a]	
			36 41 51
KvAP (1ORQ)	P	183	VFDAL WWAVVTATTV GYGDVVP
$Ca_v1.2$	IP	379	FAFAM LTVFQCITM**E** GWTDVLY
	IIP	722	FPQSL LTVFQILTG**E** **D**WNSVMY
	IIIP	1131	VLAAM MALFTVSTF**E** GWPELLY
	IVP	1432	FPQAV LLLFRCATG**E** AWQDIML
$Na_v1.4$	IP	386	FSWAF LALFRLMTQ**D** YWENYSP
	IIP	741	FFHSF LIVFRILCG**E** WIETYSP
	IIIP	1223	VGLGY LSLLQVATF**K** GWMDYSP
	IVP	1515	FGNSI ICLFEITTS**A** GWDGYSP
			1 11
KvAP	S6	207	PIGKVIGIAV MLTGI
$Ca_v1.2$	IS6	409	ELPWVYFVSL VIFGS
	IIS6	757	MLVCIYFIIL FICGN
	IIIS6	1170	VEISIFFIIY IIIIA
	IVS6	1480	SFAVFYFISF **Y**MLCA

[a] KvAP residues are numbered as in the X-ray structure (PDB index 1ORQ). The UniProt residue numbers are used for $Na_v1.4$ (P15390) and $Ca_v1.2$ (P15381)

The channel model was Monte Carlo-minimized in four stages with an increasing number of degrees of freedom: (1) torsional angles not defined in the template structures, (2) all side-chain torsions, (3) all side-chain and backbone torsions, and (4) all variables including those governing positions and orientations of the polypeptide chains. All-trans starting torsions were assigned for side chains except for prolines. The lowest energy conformation found at the previous stage was used as the starting point for the next stage of MC minimization. The lowest energy structure

found at stage (4) was used as the starting point for the Ca^{2+} docking described under Results. The MCM calculations involved 1,000 energy minimizations in each of the first three stages. At the fourth stage, the MCM calculations were terminated when 5,000 consecutive energy minimizations did not improve (decrease) the energy of the apparent global minimum. This step-by-step relaxation prevented unrealistic deviations of the main-chain atoms from the templates, which would be caused by steric clashes. Throughout all stages, C^{α} atoms in the inner helices and in positions *p36–p46* of the P-helices were constrained by pins to the positions of the homologous atoms in the KvAP template. A pin is a flat-bottom penalty function (Brooks et al. 1985) that allows a C^{α} atom to deviate penalty-free from the template up to 1 Å and imposes a penalty with a force constant of 10 kcal mol^{-1} $Å^{-2}$ for larger deviations. C^{α} atoms at the C-ends of P-helices (positions *p47–p48*) and in the ascending limbs (positions *p52–p57*) were pinned to the $Na_v1.4$ template (Tikhonov and Zhorov 2005). No constraints were imposed on C^{α} atoms at the P-loop turns (positions *p49–p51*).

Results

Ca^{2+} docking in L-type Ca^{2+} channel

The number of Ca^{2+} ions in the outer pore and the protonation states of ionizable residues are unknown. Protons block Ca^{2+} channels and mutational data suggest that the selectivity filter glutamates cooperate in proton binding (Chen et al. 1996). A single model with a fixed number of Ca^{2+} ions and ionized residues is unlikely to explain the ion permeation. Therefore, we explored three models (Ca^{2+}-saturated, Ca^{2+}-deficient, and Ca^{2+}-excessive models) in which two or three calcium ions were added to the selectivity filter region. In all calculations, the four selectivity filter glutamates in positions *p50* (the EEEE locus) were ionized. In the Ca^{2+}-saturated model, the four negative charges of the EEEE locus were balanced by four positive charges at two Ca^{2+} ions, while other ionizable residues in the outer pore were kept neutral. The outer pore includes a highly conserved aspartate D^{2p51} adjacent to the selectivity filter glutamate E^{2p50}. The role of D^{2p51} is unknown. We explored possible involvement of D^{2p51} in the ion permeation in the Ca^{2+}-deficient and Ca^{2+}-excessive models, which involved two and three calcium ions, respectively, and the ionized D^{2p51}. Besides the EEEE locus and D^{2p51}, the outer pore of $Ca_v1.2$ contains the acidic residues D^{1p54}, E^{3p54}, and D^{4p54}. These residues were considered in the protonated form only because their alpha-carbons are far (>9 Å) from alpha-carbons of E^{p50} residues in respective repeats (Fig. 2a, b).

Preliminary MC minimizations of starting points with Ca^{2+} ions randomly seeded in the selectivity filter region yielded many structures with acidic side chains trapped near the starting points due to electrostatic attractions to Ca^{2+} ions. To obtain diverse conformations of the acidic residues, Ca^{2+} ions were constrained to be within 4.6 Å from carboxylate carbons according to one of the patterns shown in Table 2. These patterns represent all possibilities in which a Ca^{2+} ion is constrained to a pair of glutamates, but no glutamate is constrained to two Ca^{2+} ions simultaneously. In the Ca^{2+}-excessive model, the third Ca^{2+} ion was constrained to the carboxylate carbon of D^{2p51}. Each pattern was explored using the multi-MCM protocol similar to that described in the accompanying paper (Cheng and Zhorov 2009). In the first stage, 100,000 starting points were generated with random positions of Ca^{2+} ions, random conformations of side chains in positions *p48–p52*, and Ca^{2+}-carboxylate constraints corresponding to the given pattern. A starting point was relaxed in a 20-step MCM. Structures within 200 kcal/mol from the apparent global minimum were collected and clustered as described in (Cheng and Zhorov 2009). In the second stage, each collected structure was refined in a 1,000-step MCM still with Ca^{2+}-carboxylate constraints. In the third stage, structures within 100 kcal/mol from the apparent global minimum found in the second stage were refined without Ca^{2+}-carboxylate constraints by MC minimizations terminated when 1,000 consecutive steps did not improve the apparent global minimum. Energetically unfavorable Ca^{2+}-protein complexes, which may have been imposed by Ca^{2+}-carboxylate constraints, were rejected in the last, unconstrained MCM. During MC minimizations, all the torsions (both sampled and not sampled) were optimized. The comprehensive sampling of the starting points and optimization of all torsions minimized the dependence of the side-chain conformations in the Ca^{2+}-bound channel on the initial channel model described in "Methods".

Distributions of Ca^{2+} ions and carboxylates

To describe our results in geometric terms, we define a coordinate system with the extracellularly directed *z*-axis that coincides with the pore axis, the *xy*-plane drawn via C^{α} atoms in positions *p50*, and angle θ between the line drawn via two Ca^{2+} ions and the *xy*-plane (Fig. 2b, c). For example, $\theta = 90^{\circ}$ when a line between two Ca^{2+} ions is parallel to the *z*-axis and $\theta = 0^{\circ}$ when the line is parallel to the *xy* plane. In the Ca^{2+}-excessive model, θ values were calculated for the pair of Ca^{2+} ions that are most distant from each other. The condition that the Ca^{2+}-O distance $\leq$2.8 Å was used as a criterion of a Ca^{2+}-coordinating bond because Ca^{2+}-O distances as large as 2.7 Å are observed in X-ray structures (Harding 2002, 2006).

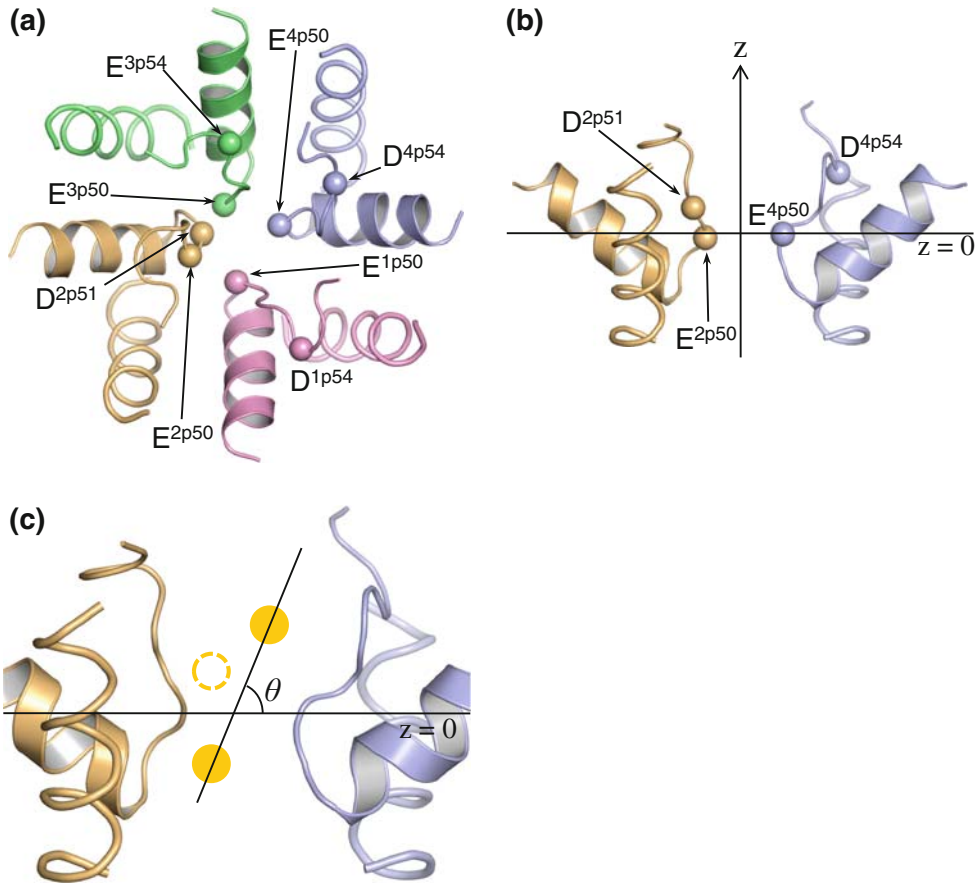

Fig. 2 The $Ca_v1.2$ outer pore model with repeats I, II, III, and IV colored *pink*, *orange*, *green*, and *blue*, respectively. Alpha-carbons of the selectivity filter glutamates (E^{p50}s), D^{2p51}, and acidic residues in positions *p54* are shown as *spheres*. **a** Extracellular view. **b** Side view with the *xy*-plane and the *z*-axis. **c** Definition of angle θ

Table 2 Ca^{2+}-carboxylate constraints used in calculations

Ca^{2+}-saturated and deficient[a] models	
Pattern 1	E^{1p50}–Ca^{2+}–E^{2p50}; E^{3p50}–Ca^{2+}–E^{4p50}
Pattern 2	E^{1p50}–Ca^{2+}–E^{3p50}; E^{2p50}–Ca^{2+}–E^{4p50}
Pattern 3	E^{1p50}–Ca^{2+}–E^{4p50}; E^{2p50}–Ca^{2+}–E^{3p50}
Ca^{2+}-excessive model	
Pattern 1	E^{1p50}–Ca^{2+}–E^{2p50}; E^{3p50}–Ca^{2+}–E^{4p50}; D^{2p51}–Ca^{2+}
Pattern 2	E^{1p50}–Ca^{2+}–E^{3p50}; E^{2p50}–Ca^{2+}–E^{4p50}; D^{2p51}–Ca^{2+}
Pattern 3	E^{1p50}–Ca^{2+}–E^{4p50}; E^{2p50}–Ca^{2+}–E^{3p50}; D^{2p51}–Ca^{2+}

[a] Residue D^{2p51} is ionized in Ca^{2+}-deficient models, but not constrained to any Ca^{2+} ion

The three-stage MC minimization of the Ca^{2+}-saturated model yielded an ensemble of 155 structures in which Ca^{2+} ions bind to side chains of E^{p50}s and some main-chain oxygens. Fig. 3a and b shows a superposition of the Ca^{2+} ions of the 155 structures. Within the ensemble, *z*-coordinates of Ca^{2+} ions vary from −2.7 to 6.3 Å, the ions deviate up to 7 Å from the *z*-axis, and angels θ vary from 1° to 85° (Fig. 4a, b, d). In most structures, the distance between two Ca^{2+} ions range from 3.7 to 9 Å, but distances up to 11 Å are found (Fig. 4c). The Ca^{2+}-coordination number (i.e., the number of oxygens within 2.8 Å from Ca^{2+}) varies from 4 to 7, with an average of 5.4 per Ca^{2+} ion. A Ca^{2+} ion forms an average of 3.5 and 1.8 coordinating bonds, respectively, with the side-chain and main-chain oxygens. Notably, calculations did not predict any dominant Ca^{2+}-binding pattern in the ensemble and characteristics of the complexes are distributed rather smoothly (Fig. 4).

MC minimizations of the Ca^{2+}-deficient and Ca^{2+}-excessive models yielded ensembles of 32 and 30 structures, respectively. Distributions of characteristics in these ensembles are sharper than in the Ca^{2+}-saturated ensemble, possibly due to the smaller number of structures. In the Ca^{2+}-deficient ensemble, Ca^{2+} ions deviate up to 6 Å from the *z*-axis, the *z*-coordinate varies from −0.3 to 6.5 Å, distances between Ca^{2+} ions vary from 4.1 to 5.7 Å, and angle θ varies from 2 to 72° (Fig. 4). Ca^{2+}-coordinating number averages 5.6 per ion. Each Ca^{2+} ion forms an average of 3.6 and 2.0 coordinating bonds, respectively, with the side-chain and main-chain oxygens. The geometric diversity of the collected structures is similar to that in the Ca^{2+}-saturated model. In the Ca^{2+} excessive model, Ca^{2+} ions deviate up to 6 Å from the *z*-axis and have *z*-coordinates from −1.7 to 7.7 Å. Distances between adjacent Ca^{2+} ions range from 4.0 to 8.3 Å, and θ varies from 4 to 78°. Ca^{2+} coordination number averages 5.3 per

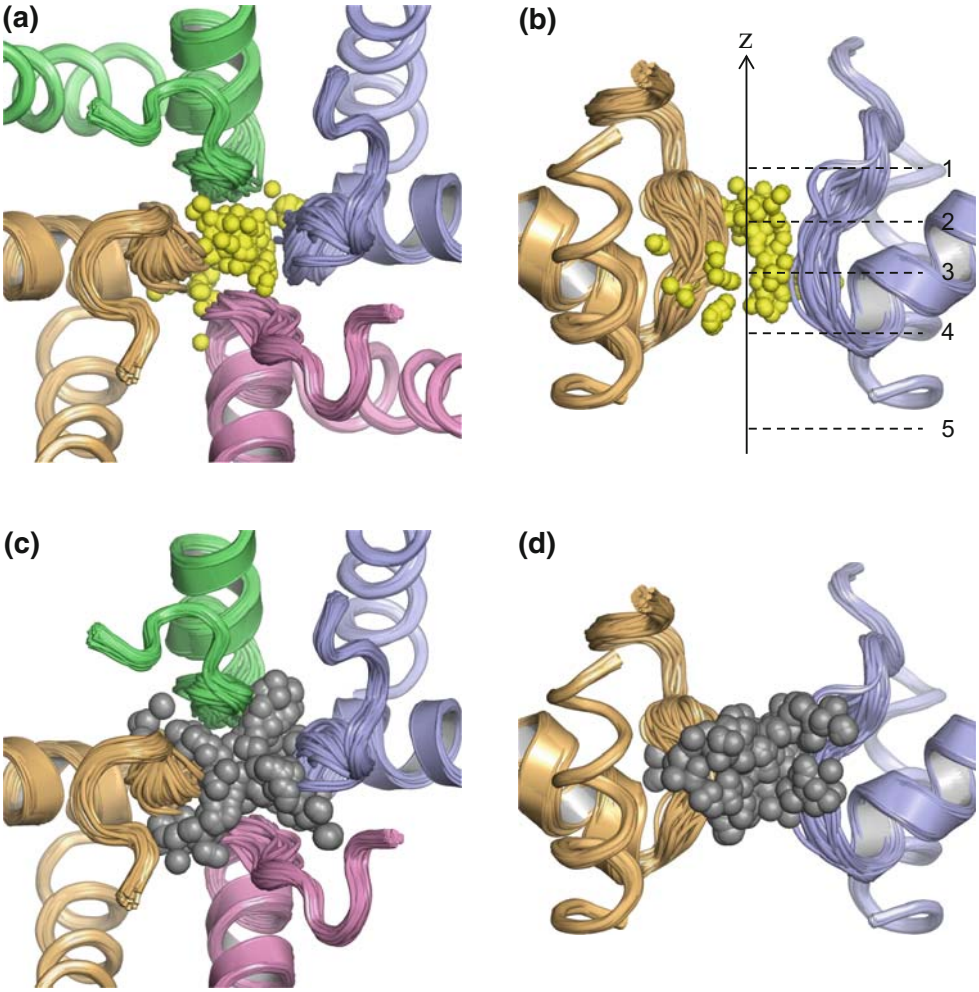

Fig. 3 Distributions of Ca^{2+} ions and carboxylate carbons. Repeats are *colored* as in Fig. 2. **a** and **b** Extracellular and side views of the superposition of Ca^{2+} ions in 155 structures of the Ca^{2+}-saturated ensemble. *Numbered horizontal lines* (**b**) mark the outer pore levels that correspond to K^+ sites in KvAP. **c** and **d** Extracellular and side view of carboxylate-carbons in 155 structures in the Ca^{2+}-saturated model

Ca^{2+} ion. Each Ca^{2+} ion forms an average of 3.2 and 2.2 coordinating bonds, respectively, with the side-chain and main-chain oxygens. Compared to other ensembles, in the Ca^{2+}-excessive ensemble Ca^{2+} ions are farther from the z-axis (Fig. 4b), and hence backbone oxygens coordinate Ca^{2+} ions more frequently. Angle θ in the Ca^{2+}-saturated and Ca^{2+}-deficient ensembles is widely distributed (Fig. 4d), but in most of the Ca^{2+}-excessive structures, $40^\circ < \theta < 50^\circ$. (In a Ca^{2+}-excessive structure, θ was measured using a pair of atoms that are most distant from each other. The diversity of θ values in the Ca^{2+}-saturated ensemble is smaller than in other ensembles regardless of how θ is measured.) Thus, our calculations predicted many possible Ca^{2+}-binding modes with various inter-Ca^{2+} distances, deviations of Ca^{2+} ions from the z-axis and xy-plane, and angles θ. The protonation state of D^{2p51} does not markedly affect Ca^{2+} distribution (characteristics of the Ca^{2+} saturated and Ca^{2+} deficient models are similar), whereas the third ion in the Ca^{2+} excessive model significantly affects Ca^{2+} distribution (Fig. 4). In the Ca^{2+}-saturated and deficient ensembles, most of the Ca^{2+} ions are close to the pore axis, but some ions occur in interfaces between repeats (Figs. 3a, 4b). In the Ca^{2+}-excessive ensemble, most Ca^{2+} ions are far from the pore axis (Fig. 4b).

As expected, flexible side chains of E^{p50}s adopted many different conformations in the ensembles (Fig. 3c). Since practically in all structures every acidic residue is involved in Ca^{2+} coordination, distribution of carboxylates in the pore (Fig. 3c, d) is similar to that of Ca^{2+} ions (Fig. 3a, b). Practically all the outer pore lumen is populated by Ca^{2+}-coordinating carboxylates. This cloud-like distribution of the selectivity filter carboxylates is in sharp contrast with immobile backbone carbonyls in the selectivity filter of K^+ channels. This result supports the "electric stew" concept of the selectivity filter region (McCleskey 2000), which is used in theoretical studies of Ca^{2+} permeation (Nonner et al. 2000; Corry et al. 2001; Boda et al. 2007; Boda et al. 2008; Gillespie and Boda 2008).

No carboxylate was simultaneously constrained to two Ca^{2+} ions (Table 2), but in 131 structures of the Ca^{2+}-saturated ensemble at least one carboxylate forms a

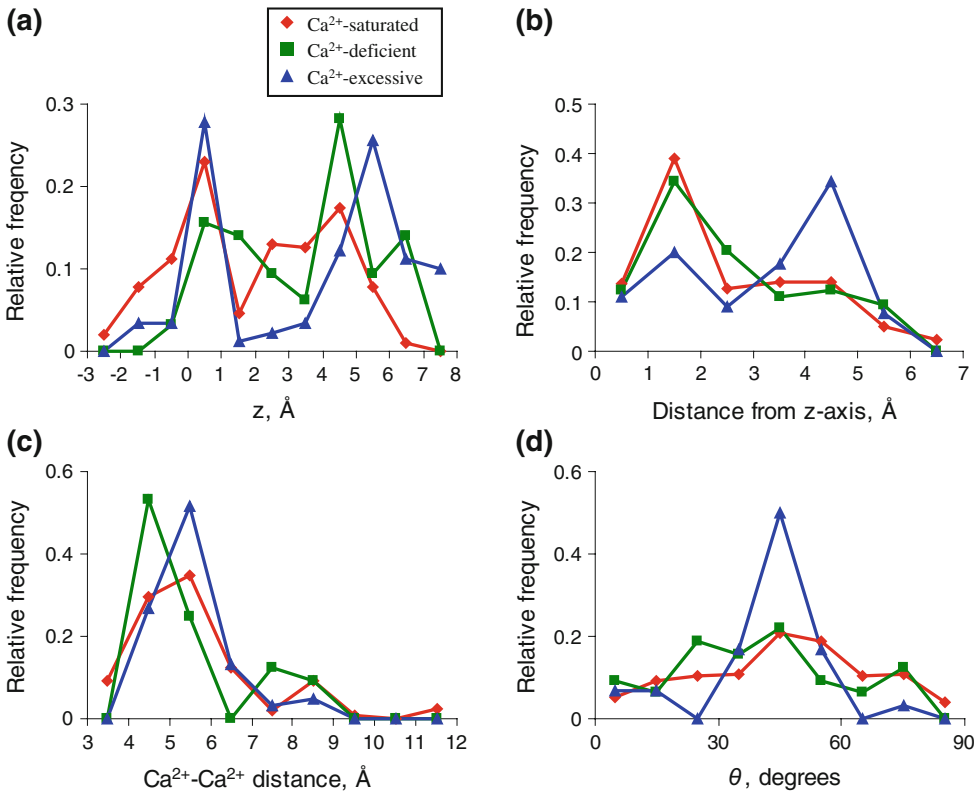

Fig. 4 Distributions of geometric characteristics of Ca^{2+} ions: Ca^{2+}-saturated (*red diamonds*), Ca^{2+}-deficient (*green squares*), and Ca^{2+}-excessive (*blue triangles*) ensembles. A relative frequency (ordinate) is the number of structures with the specific characteristic divided by the total number of structures in the ensemble. **a** The z coordinates of Ca^{2+} ions. **b** Distances of Ca^{2+} ions from the z-axis. **c** Distances between Ca^{2+} ions. For the Ca^{2+}-excessive ensemble plotted are the two shortest among three possible Ca^{2+}-Ca^{2+} distances. **d** Angle θ. For the Ca^{2+}-excessive ensemble, θ is defined for the pair of most distant Ca^{2+} ions

"bridge" between Ca^{2+} ions. A carboxylate group is considered bridging if it coordinates two Ca^{2+} ions simultaneously (Ca^{2+}-O distances $\leq$2.8 Å). Bridging carboxylates are seen in X-ray structures of some Ca^{2+}-binding proteins (Harding 2006). Up to four bridging glutamates are found in the Ca^{2+}-saturated ensemble (Fig. 5). Ca^{2+}-deficient and Ca^{2+}-excessive ensembles also contain many bridging carboxylates (not shown). The distances between bridged Ca^{2+} ions is small (4–6 Å), while in structures without bridging glutamates, Ca^{2+} ions are up to 12 Å apart.

Repeats of the L-type Ca^{2+} channel have different sequences (Table 1). Besides the sequential asymmetry, our homology model inherited structural asymmetry of the P-loops region from the Na^{+} channel model (Tikhonov and Zhorov 2005, 2007). Therefore, asymmetry of coordination patterns and ion distributions are unsurprising. The most obvious asymmetry was introduced by the charged D^{2p51} residue in Ca^{2+}-deficient and Ca^{2+}-excessive ensembles. D^{2p51} coordinates Ca^{2+} in all structures of the Ca^{2+} excessive ensemble. In ~50% structures of the Ca^{2+}-deficient ensemble, D^{2p51} turns away from the pore lumen and does not participate in Ca^{2+} coordination. In the Ca^{2+}-excessive ensemble, D^{2p51} bridged Ca^{2+} ions in 70% of structures and coordinated the top (most extracellular) and the middle Ca^{2+} ions in 69 and 88% of structures, respectively. In other words, D^{2p51} usually "welcomes" an incoming Ca^{2+} ion to the selectivity filter region. By contrast, D^{2p51} rarely coordinates Ca^{2+} in the Ca^{2+}-deficient ensemble, indicating that when the most cytoplasmic Ca^{2+} leaves the selectivity filter to the inner pore, the incoming Ca^{2+} ion moves from D^{2p51} to E^{p50}s. The Ca^{2+}-Ca^{2+} repulsion results in the tendency to maximize the distance between Ca^{2+} ions. As a consequence, in the Ca^{2+}-excessive ensemble we often see diagonal distribution of Ca^{2+} ions with the most extracellular ion coordinated by D^{2p51} and the most intracellular ion located near the interface of repeats III and IV. Such an arrangement is an important feature of the permeation mechanism proposed in a later section.

Energetic characteristics of the models

Energetic and geometric characteristics of the complexes strongly depend on the number of bridging carboxylates. Structures with different numbers of bridging carboxylates have clearly distinct energetic and geometric characteristics (Fig. 6). This allows to categorize the structures according to the number of bridging carboxylates and to calculate average parameters for each category (Table 3). Compared to unbridged Ca^{2+} ions, the bridged ones are closer to each other and repel more strongly from each other (Fig. 6a), especially when Ca^{2+} ions are bridged by three or four carboxylates (Fig. 6a). Repulsion between the carboxylates also increases with the number of bridging

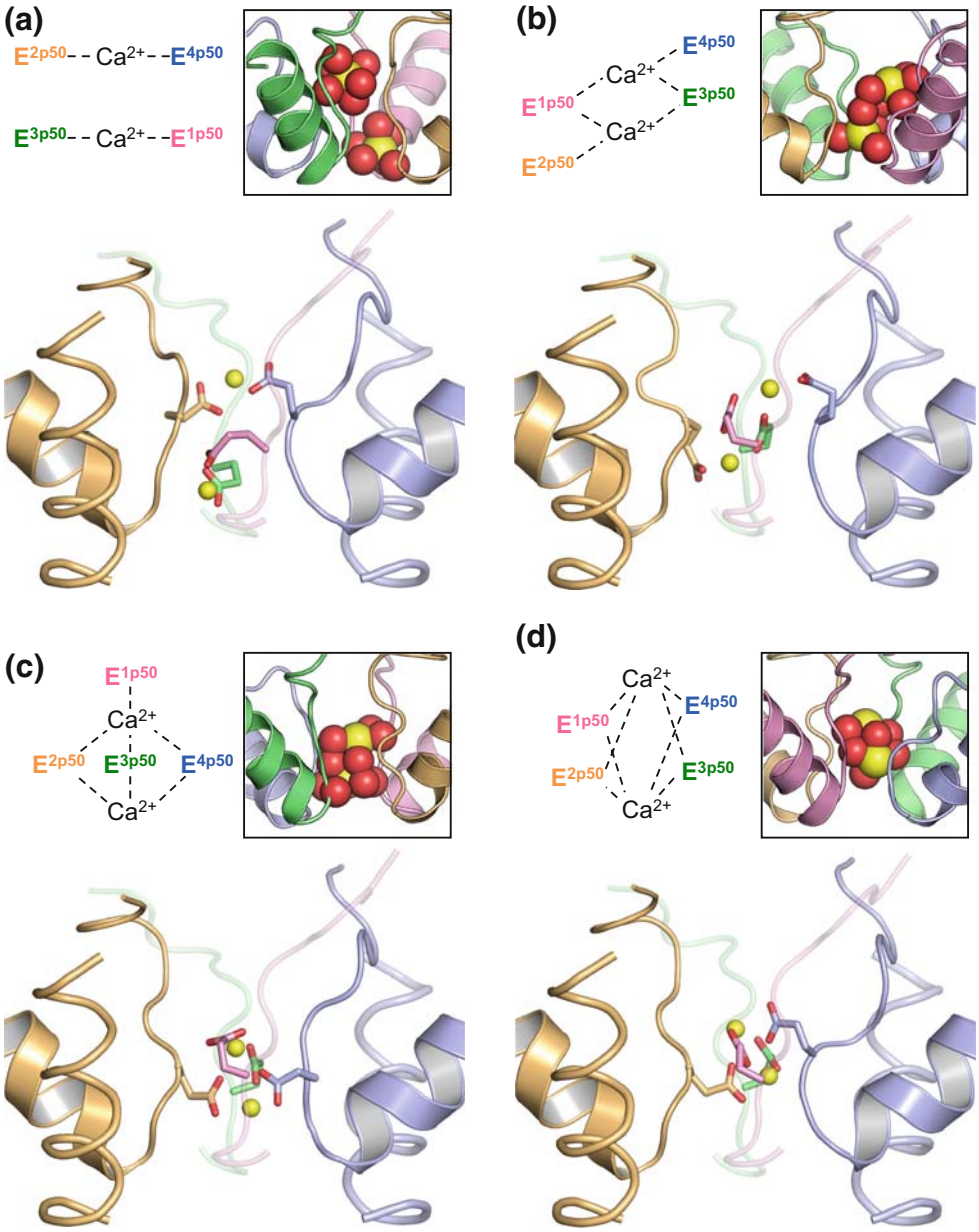

Fig. 5 Structures of the outer pore and corresponding schemes of Ca^{2+} binding from the Ca^{2+}-saturated ensemble with zero (**a**), two (**b**), three (**c**), and four (**d**) bridging carboxylates and schemes of respective patterns of Ca^{2+} coordination. Repeats are *colored* as in Fig. 2. The selectivity filter glutamates are shown as *sticks*. For clarity, only those Ca^{2+}-coordinating bonds that involve side chains of the selectivity filter glutamates (*sticks*) are shown. Insets show all Ca^{2+}-coordinating oxygens (*red spheres*) in respective structures. The insets are oriented to provide the best view for Ca^{2+} coordination

carboxylates (Fig. 6c). However, the electrostatic repulsions are counterbalanced by stronger attractions between Ca^{2+} ions and the carboxylates (Fig. 6b). In structures without bridging carboxylates, the distances between Ca^{2+} ions are larger and therefore inter-Ca^{2+} and inter-carboxylate repulsions are weaker than those in the complexes with the bridging carboxylates (Fig. 6). However, the electrostatic attractions in these structures are also relatively weak. Thus, if we consider only carboxylates and Ca^{2+} ions, our calculations particularly favor complexes with Ca^{2+} ions bridged by two or three carboxylates (Fig. 6d). On the other hand, the coordination number of Ca^{2+} ions and the energy of Ca^{2+} interactions with the outer pore residues in positions *p48–p52* do not depend on the number of bridging carboxylates (Table 3; Fig. 6e). In the structures without bridging carboxylates, the Ca^{2+} ions approach the channel walls and strongly interact with the pore-facing backbone carbonyls. As a result, the total energy of the outer pore with Ca^{2+} ions does not depend on the number of bridging carboxylates (Fig. 6e; Table 3).

In other ensembles the trends are similar except for obvious increase of Ca^{2+}–Ca^{2+} repulsions in the Ca^{2+}-excessive model (not shown). The negative charge at D^{2p51} increases the inter-carboxylate repulsions in the Ca^{2+}-excessive and Ca^{2+}-deficient models. In a representative structure from the Ca^{2+}-excessive ensemble (Fig. 7a), the top, middle, and bottom Ca^{2+} ions have energies of -77 ± 16, -122 ± 8, and -103 ± 15 kcal/mol, respectively. This trend is consistent

with the "stair-step" mechanism (Kuo and Hess 1993b) according to which a high-affinity Ca^{2+}-binding site is flanked by two lower-affinity Ca^{2+}-binding sites.

Lipkind and Fozzard designed a model with four E^{p50}s symmetrically arranged around three Ca^{2+} ions arranged single file with the central Ca^{2+} ion octacoordinated by the four E^{p50}s (Lipkind and Fozzard 2001). Such a structure was not found in our ensembles. We attempted to construct this model by constraining three Ca^{2+} ions to four E^{p50}s. Intensive MC minimization of the constrained structure yielded a complex with the distances between adjacent Ca^{2+} ions <3 Å and strong Ca^{2+}-Ca^{2+} repulsions. This structure was unstable upon removal of the constraints. Another model with a single Ca^{2+} ion octacoordinated by the selectivity filter glutamates (Lipkind and Fozzard 2001) was also unstable upon removal of Ca^{2+}-glutamate constraints. However, we found low-energy structures with two Ca^{2+} ions bridged by the four glutamates (Fig. 5d) in a manner that resembles the model of Lipkind and Fozzard from which the middle Ca^{2+} is removed.

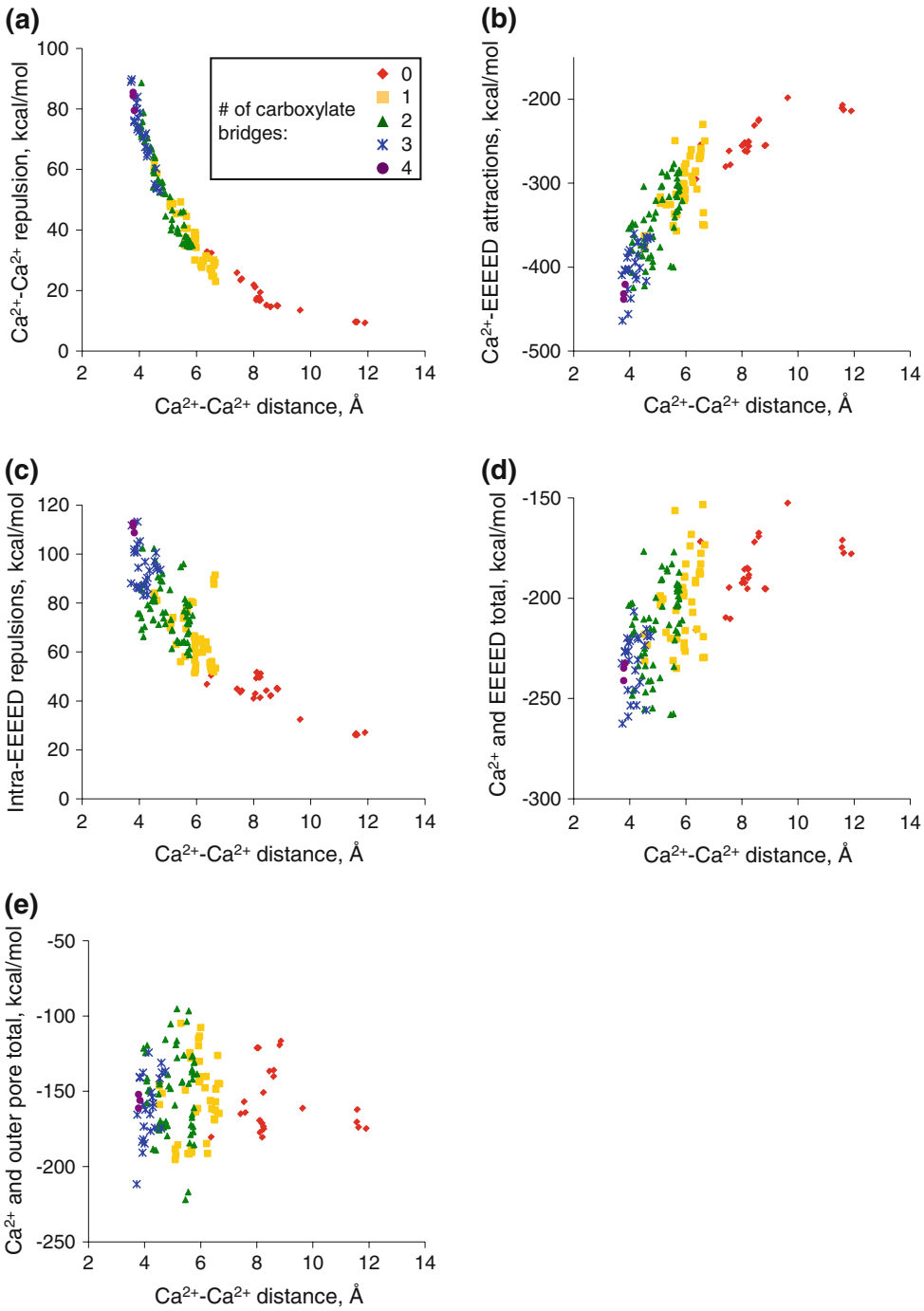

Fig. 6 Energy (kcal/mol) of structures from the Ca^{2+}-saturated ensemble plotted against inter-Ca^{2+} distance: Ca^{2+}-Ca^{2+} repulsion (**a**), Ca^{2+}-EEEED interactions (**b**), EEEED internal repulsions (**c**), total Ca^{2+}-EEEED energy (**d**), and total energy of Ca^{2+} ions and outer pore residues (p48 to p52) (**e**). The number of bridging carboxylates is *color-coded*. Distance between bridged Ca^{2+} ions cannot exceed 7 Å. Ca^{2+}-EEEED energy decreases with the number of bridges because Ca^{2+}-EEEED attractions are stronger than inter-Ca^{2+} (**a**) and inter-carboxylate (**c**) repulsions. Such a tendency is lost when the energy of Ca^{2+} attraction to the backbone carbonyls is included (**e**)

Table 3 Characteristics of the Ca^{2+}-saturated ensemble

	Number of bridging carboxylates				
	0	1	2	3	4
Number of					
Structures in the ensemble	24	43	60	25	3
Side chain oxygens, per $2Ca^{2+}$	5.5 ± 1.6	5.7 ± 1.1	6.9 ± 0.9	8.6 ± 1.1	9.3 ± 0.6
Backbone oxygens, per $2Ca^{2+}$	4.5 ± 0.7	3.8 ± 0.9	2.8 ± 0.7	2.5 ± 0.2	0.3 ± 0.6
Protein oxygens, per $2Ca^{2+}$	10.0 ± 2.0	9.5 ± 1.2	9.7 ± 1.0	11.1 ± 1.4	9.7 ± 0.6
Protein oxygens, per Ca^{2+}	5.0 ± 1.2	4.8 ± 1.1	4.8 ± 0.8	5.5 ± 1.0	4.8 ± 0.4
Energy (kcal/mol)					
Ca^{2+}-Ca^{2+} repulsion, per Ca^{2+}	8.9 ± 3.2	18.5 ± 5.0	25.3 ± 7.4	35.4 ± 5.2	41.6 ± 1.6
Ca^{2+}-EEEED[a], per Ca^{2+}	−123.0 ± 12.5	−153.0 ± 17.6	−170.5 ± 20.2	−199.1 ± 13.9	−215.1 ± 4.5
EEEED (intra-locus)	42.2 ± 8.4	66.7 ± 11.5	76.5 ± 10.4	94.8 ± 8.4	111.0 ± 2.1
Subset (EEEED + $2Ca^{2+}$)	−185.9 ± 14.9	−202.4 ± 20.9	−214.0 ± 22.0	−232.5 ± 15.4	−236.1 ± 4.5
Subset (outer pore[b] + $2Ca^{2+}$)	−156.1 ± 8.4	−154.6 ± 25.3	−150.6 ± 27.2	−160.6 ± 21.4	−156.3 ± 4.6
Ca^{2+} distance from axis *z* (Å)	3.9 ± 1.8	2.8 ± 1.5	2.3 ± 1.3	1.4 ± 0.6	1.3 ± 0.2

[a] Energy of interaction of Ca^{2+} ions with the EEEED locus

[b] Twenty residues (positions *p48* through *p52* of the four repeats)

Possible mechanism of Ca^{2+} permeation

Our results do not support the permeation mechanism proposed by Lipkind and Fozzard (2001). The collected ensembles of MC-minimized structures allow us to propose an alternative mechanism illustrated in Fig. 7. The structure in Fig. 7a has been selected from the Ca^{2+}-excessive ensemble. An ion incoming from the extracellular space would bind to D^{2p51}, a highly conserved residue adjacent to E^{2p50}. This Ca^{2+} ion brings an excessive positive charge to the selectivity filter region and thus induces the release of a Ca^{2+} ion at the cytoplasmic side of the selectivity filter. Upon release of the excessive Ca^{2+} ion, the selectivity filter becomes Ca^{2+}-deficient. Therefore, we selected other snapshots from the Ca^{2+}-deficient ensemble to further illustrate the proposed mechanism of Ca^{2+} permeation (Fig. 7b–d). According to this mechanism, the side chain of D^{2p51} would turn away from the pore axis, and the system becomes similar to the Ca^{2+}-saturated model in which D^{2p51} is protonated and four E^{p50}s neutralize two Ca^{2+} ions. Thus, D^{2p51} is essential for binding of incoming Ca^{2+} ions, but does not participate in subsequent steps of the ion permeation. These steps include several transitions of two Ca^{2+} ions towards the cytoplasm. Importantly, two or three bridging glutamates are involved in each step of the permeation process as illustrated in Fig. 7b–d. We suggest that the bridging glutamates are the key determinants of the mechanism of Ca^{2+} permeation. Notably, the non-bridging glutamate in Fig. 7b is intracellular, whereas the non-bridging glutamate in Fig. 7c turns towards the outer vestibule. Finally, the system would reach the state in which the Ca^{2+} ion at the cytoplasmic side of the selectivity filter approaches the inner pore, while two glutamates at the extracellular side of the selectivity filter coordinate the upper Ca^{2+} ion and face the external vestibule (Fig. 7d). In this state, the system is ready to accept the next incoming Ca^{2+} ion and return to the initial state (Fig. 7a). Importantly, the major difference between structures *a* and *d* is the presence of the third, incoming Ca^{2+} ion, which is coordinated by D^{2p51}. The essence of the proposed mechanism is the coupled movement of Ca^{2+} ions and selectivity filter carboxylates, which switch between the bridging and non-bridging Ca^{2+}-chelating modes. Obviously, in the absence of a high-resolution experimental structure of the selectivity filter, the snapshots in Fig. 7 only serve as an illustration of the proposed conceptual mechanism of Ca^{2+} permeation.

Discussion

In this study we employed the multi-MCM protocol to predict possible patterns of Ca^{2+}-coordination in the selectivity filter region of the L-type Ca^{2+} channel. The calculations yielded ensembles of structures, which were used to describe the possible mechanism of ion permeation. To our knowledge, this is the first attempt to elaborate this mechanism at the atomic-scale level. Earlier models of the selectivity filter were either static (Lipkind and Fozzard 2001; Zhorov et al. 2001) or did not consider atomic details (Corry et al. 2001; Boda et al. 2007; Boda et al. 2008).

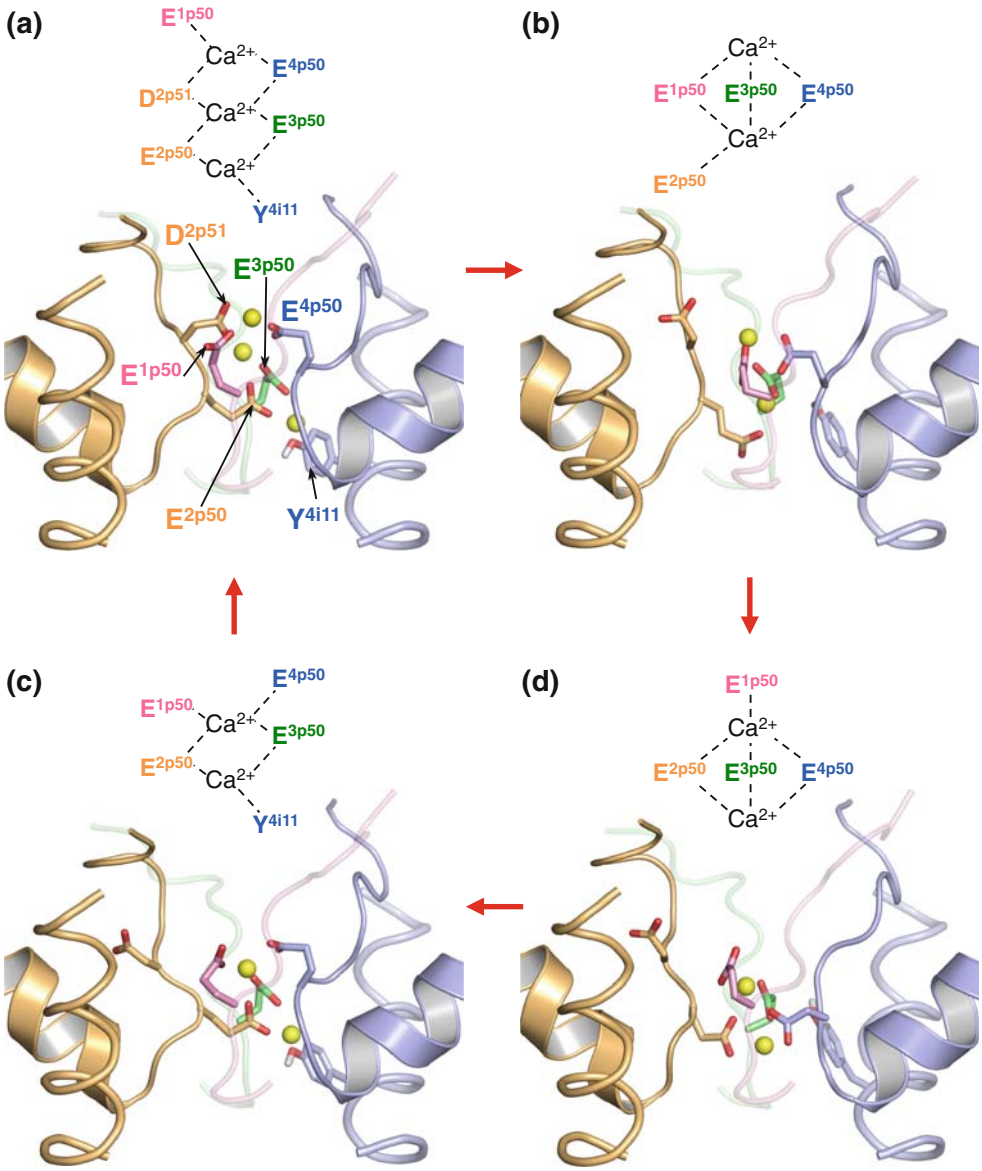

Fig. 7 The proposed mechanism of Ca^{2+} permeation through the selectivity filter region. Side chains of E^{p50}s, D^{2p51}, and Y^{4i11} are shown as sticks. Repeats are colored as in Fig. 2. The pattern of Ca^{2+}-coordination by the EEEED locus and Y^{4i11} is shown schematically at the *top* of each *panel*. See text for the description of the permeation mechanism

Characteristics of Ca^{2+}-channel complexes

The Ca^{2+}-coordination number in proteins typically varies from six to eight (Katz et al. 1996; Harding 2001), whereas the average coordination number in our model was 5.4. Additional Ca^{2+}-coordinating ligands are likely water molecules, whose energy contributions were taken into account by the implicit solvent method. Along with side-chain oxygens, backbone oxygens (mostly from positions *p48–p52*) contribute to Ca^{2+} binding in our models. Involvement of backbone oxygens in Ca^{2+}-coordination is unsurprising because the eight sidechain oxygens of the EEEE locus are insufficient to fill the first coordination spheres of two Ca^{2+} ions. Interestingly, residues immediately N-terminal to E^{1p50} and E^{3p50} and residues C-terminal to E^{2p50} and E^{4p50} are glycines whose backbone oxygens can readily participate in the Ca^{2+} coordination. This is consistent with the observation that the glycine content adjacent to Ca^{2+}-binding residues is about twice as large as the average glycine content in proteins (Harding 2004).

Several studies, e.g., (Boda et al. 2006) consider the carboxylate oxygens of the selectivity filter glutamates as an "electric stew" (McCleskey 2000) in a low-dielectric environment. Our results, which show high mobility of Ca^{2+} ions and carboxylates, are consistent with this concept, but they also provide snapshots of structures mixed up in the "electric stew." For the electrical stew model, the dielectric constant of 5 was found optimal to explain the affinity of the selectivity filter glutamates for Ca^{2+} ions and the channel selectivity for Ca^{2+} over Na^{+} (Boda et al. 2006). Instead of a constant value of dielectric permittivity, we employed a dielectric function, which returns a dielectric permittivity in

the range of 2.3–8.4 for Ca^{2+}-oxygen contacts depending on distance between the contacting atoms and their exposure to the solvent. This implicit-solvent approach was validated by predicting Ca^{2+} binding to various proteins (Cheng and Zhorov 2009).

In some of the collected structures, a Ca^{2+} ion is in the lower level of the outer pore, which is equivalent to site 4 in the selectivity filter of K^+ channels (Fig. 3b). This site is reachable by inner-pore blockers of K^+ channels (Bruhova and Zhorov 2007; Lerche et al. 2007). In our present model, the Ca^{2+} ion at this level is not screened from the inner pore by the ascending limbs and therefore can directly interact with the inner-pore ligands as proposed in our recent models of $Ca_v1.2$ with benzothiazepines (Tikhonov and Zhorov 2008), dihydropyridines (Tikhonov and Zhorov 2009), and phenylalkylamines (Cheng et al. 2009).

The ion permeation model

Experiments on the Ca^{2+} block of the Li^+ current suggest that the LTCC pore has a set of high-affinity Ca^{2+}-binding sites separated by insignificant energy barriers (Kuo and Hess 1993b). Data on the Ba^{2+} current block by Cd^{2+} further suggest that the set of high-affinity sites can simultaneously accommodate two divalent cations (Kuo and Hess 1993a). Further studies of the Li^+ current block by Ca^{2+} in double-alanine mutants of the EEEE locus and the Ba^{2+} current block by Cd^{2+} in single mutants suggest that the EEEE locus can bind more than one divalent cation, but the divalent binding sites are not independent (Ellinor et al. 1995). Our models are consistent with these results. Indeed, the predicted ensembles show multiple binding patterns between Ca^{2+} ions and the EEEED locus, and various Ca^{2+}-binding patterns may switch via intermediate structures with multiple carboxylate bridges. Our calculations predicted significant interactions between bridged Ca^{2+} ions (Fig. 6a), implying that Ca^{2+} binding to individual sites is not independent.

In the model of Lipkind and Fozzard, the ions permeate through the static, immobile ring of glutamates (Lipkind and Fozzard 2001). In contrast, the essence of our model is the dynamic rearrangement of the selectivity filter glutamates during ion permeation. In this regard, our model is more consistent with the theoretical studies (Nonner et al. 2000; Boda et al. 2007) where free-floating acidic groups are used to explain major electrophysiological properties of Ca^{2+} channels. Flexibility of the selectivity filter was also proposed to explain the increased selectivity of divalent over monovalent cations (Gillespie 2008). However, it should be emphasized that in the absence of an X-ray structure of a Ca^{2+} channel, any proposal of atomic-scale mechanisms of ion permeation should be considered as speculative and treated with caution.

Asymmetry of the selectivity filter

P-loop turns and ascending limbs of Ca^{2+} channels contain residues that differ in the four repeats (Table 1). Besides the EEEE locus, the outer pore contains other acidic residues, but only the highly conserved D^{2p51} is close to the locus. This sequential asymmetry implies functional asymmetry. In our proposed mechanism of ion permeation, two asymmetric features are obvious: binding of the incoming Ca^{2+} ion to D^{2p51} and leaving of the ion at the III/IV repeat interface. In the Ca^{2+}-excessive ensemble, the most cytoplasmic Ca^{2+} ion frequently binds to Y^{4i11}, which could facilitate Ca^{2+} transitions to the inner pore (Fig. 7). This is consistent with the proposition that Y^{4i11} plays an important role in the selectivity of ion permeation (Hockerman et al. 1995).

Numerous data show a non-equivalent contribution of the selectivity filter glutamates in the permeation and selectivity (Yang et al. 1993; Yatani et al. 1994; Parent and Gopalakrishnan 1995; Talavera et al. 2001). Asymmetry of our model generally agrees with experimental data on unequal contributions of the selectivity filter glutamates in the ion permeation. An attempt to rationalize such quantitative details would require molecular dynamics simulations with high-resolution X-ray structures. Obviously, our homology model is not precise enough for such simulations.

Possible rearrangement of Ca^{2+}-chelating patterns upon channel inactivation

Involvement of the selectivity filter in the inactivation gating of Ca^{2+} channels has long been proposed (Brum and Rios 1987; Pizarro et al. 1989). Indeed, mutation $E^{3p50}Q$ eliminates Ca^{2+}-dependent inactivation (Zong et al. 1994), indicating that the EEEE locus plays an important role in this process. In our model of ion permeation, we considered large-θ structures to describe the single-file arrangement of Ca^{2+} ions. However, MC minimizations also predicted a number of small-θ structures in which both ions have similar z-coordinates. Some of these structures have split Ca^{2+} ions chelated by pairs of E^{p50}s and lack bridging glutamates that are required to escort Ca^{2+} towards the cytoplasm by a relay-like mechanism. Since the split structures cannot participate in the proposed permeation mechanism, we suggest that they represent impermeable configurations of the selectivity filter. A possible mechanism of transition from a permeable, single-file configuration to an impermeable, split configuration is shown in Fig. 8. All the frames for this figure are taken from the Ca^{2+}-saturated ensemble. Two carboxylate-bridged Ca^{2+} ions at the pore axis (Fig. 8a) can rearrange to a smaller-θ (more horizontal) configuration without losing contacts

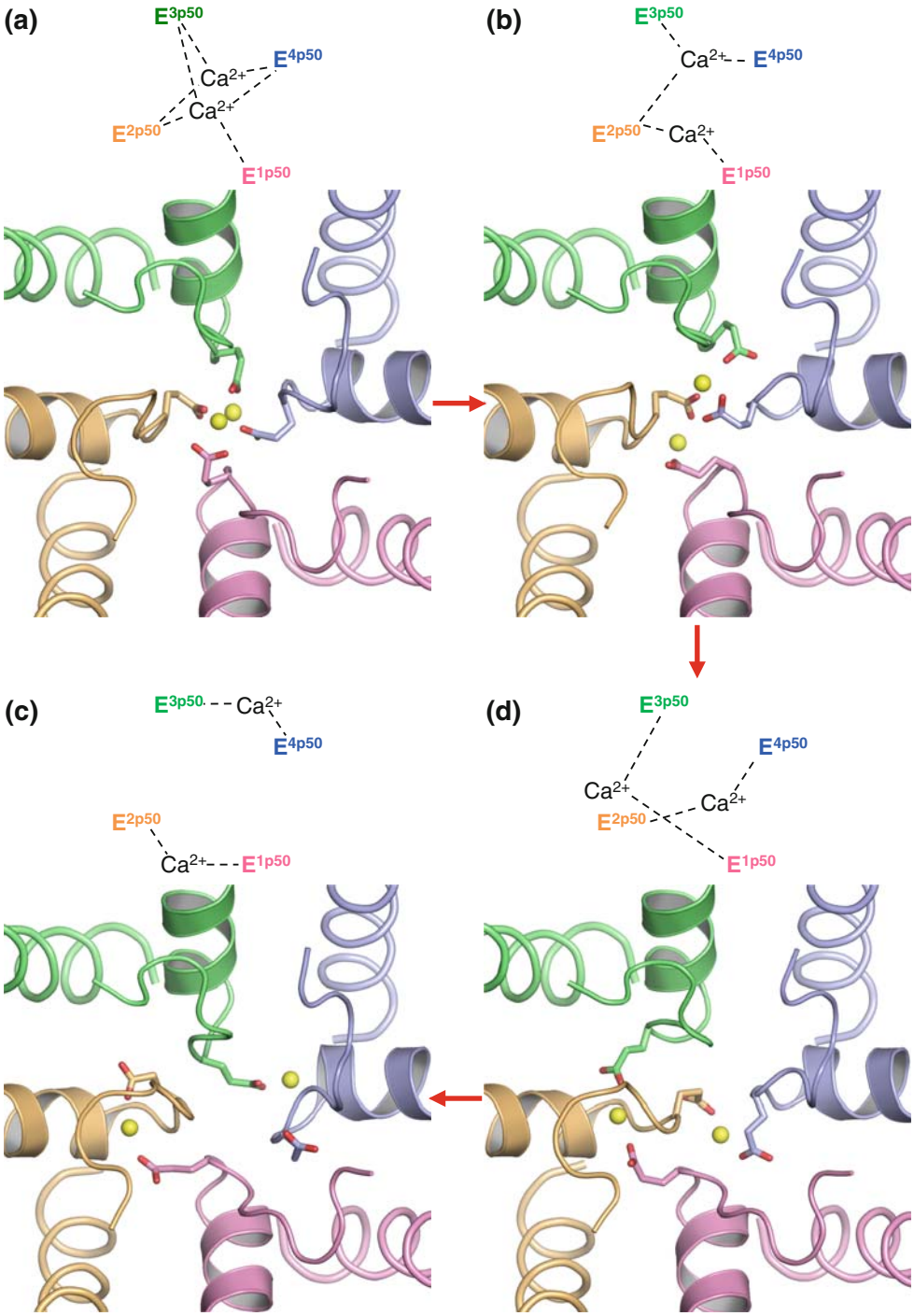

Fig. 8 Extracellular views at snapshots of possible transition from the permeating (**a**) to non-permeating (**d**) states of the selectivity filter. The pattern of Ca^{2+}-coordination by the selectivity filter glutamates is shown schematically at the *top* of each *panel*

with the bridging carboxylates (Fig. 8b). Next, separation of the Ca^{2+} ions would be coupled to the destruction of the carboxylate bridges (Fig. 8c) and would finally lead to a structure with split Ca^{2+} ions (Fig. 8d). In this structure the two Ca^{2+} ions are 11.7 Å apart.

We propose that disruption of Ca^{2+} bridging by selectivity filter carboxylates is coupled to the interruption of ion flow. Recently, Gd^{3+} binding and Ca^{2+}-dependent inactivation were demonstrated to be mutually exclusive processes that occur at the same site of Ca^{2+} channel (Babich et al. 2007). Binding of trivalent Gd^{3+} most likely requires direct interaction with three acidic residues. Such complexes would be possible in our model of ion permeation (Fig. 7), but are unlikely in the non-permeating model in which the selectivity filter glutamates are split in two distant Ca^{2+}-bound pairs (Fig. 8). We propose that the ion impermeability of the inactivated channel is caused by a loss of cooperation between the selectivity filter

glutamates rather than by a steric collapse of the pore. A similar idea that slow inactivation does not involve a steric collapse of the outer pore is elaborated in our model of the slow-inactivated Na^+ channel (Tikhonov and Zhorov 2007). Thus, our split structures may represent intermediate steps of the complex process of inactivation. Rearrangement of outer pore backbones upon Ca^{2+}-dependent inactivation may stabilize split structures, but in the absence of experimental constraints, we did not explore this possibility.

Modeling limitations

Obvious limitations of our modeling study should be emphasized. *First,* the absolute energies of Ca^{2+}-protein interactions are unrealistic and should be considered just as scoring functions. This limitation precludes predicting channel properties such as ion selectivity. *Second,* our calculations predict multiplicity of Ca^{2+} binding patterns, their asymmetry, distribution of Ca^{2+} ions along and across the pore axis, and a possibility of rearrangement of Ca^{2+}-binding patterns, but the limited precision of homology modeling does not allow us to favor specific Ca^{2+} binding patterns. *Third,* in this study we focused on the EEEED locus, while other ionizable residues were kept neutral to minimize their impact on Ca^{2+} binding. Therefore, the role of residues at position *p54* in the anomalous mole fraction effect (Cens et al. 2007) is not interpreted in our study. To some extent, our models are an intermediate between specific structural models, which illustrate various concepts of Ca^{2+} binding and permeation (Lipkind and Fozzard 2001; Zhorov et al. 2001), and models that explain many experimental observations, but do not provide atomistic details (Nonner et al. 2000; Corry et al. 2001; Boda et al. 2007; Boda et al. 2008). Until X-ray structures of Ca^{2+} channels become available, our models can be used for planning and rationalizing electrophysiological, mutational and ligand-binding experiments and for docking ligands in the pore region of Ca^{2+} channels with possible involvement of Ca^{2+} ions.

Acknowledgments This study was supported by the CIHR grant MOP-53229 to BSZ. Computations were made possible by the facilities of the Shared Hierarchical Academic Research Computing Network (SHARCNET: http://www.sharcnet.ca).

References

Babich O, Matveev V, Harris AL, Shirokov R (2007) Ca^{2+}-dependent inactivation of CaV1.2 channels prevents Gd^{3+} block: does Ca^{2+} block the pore of inactivated channels? J Gen Physiol 129:477–483

Boda D, Valisko M, Eisenberg B, Nonner W, Henderson D, Gillespie D (2006) The effect of protein dielectric coefficient on the ionic selectivity of a calcium channel. J Chem Phys 125:34901

Boda D, Valisko M, Eisenberg B, Nonner W, Henderson D, Gillespie D (2007) Combined effect of pore radius and protein dielectric coefficient on the selectivity of a calcium channel. Phys Rev Lett 98:168102

Boda D, Nonner W, Henderson D, Eisenberg B, Gillespie D (2008) Volume exclusion in calcium selective channels. Biophys J 94:3486–3496

Brooks CL, Pettitt BM, Karplus M (1985) Structural and energetic effects of truncating long ranged interactions in ionic polar fluids. J Chem Phys 83:5897–5908

Bruhova I, Zhorov BS (2007) Monte Carlo-energy minimization of correolide in the Kv1.3 channel: possible role of potassium ion in ligand-receptor interactions. BMC Struct Biol 7:5

Brum G, Rios E (1987) Intramembrane charge movement in frog skeletal muscle fibres. Properties of charge 2. J Physiol 387:489–517

Catterall WA, Perez-Reyes E, Snutch TP, Striessnig J (2005) International Union of Pharmacology XLVIII. Nomenclature and structure-function relationships of voltage-gated calcium channels. Pharmacol Rev 57:411–425

Cens T, Rousset M, Kajava A, Charnet P (2007) Molecular determinant for specific Ca/Ba selectivity profiles of low and high threshold Ca^{2+} channels. J Gen Physiol 130:415–425

Chen XH, Bezprozvanny I, Tsien RW (1996) Molecular basis of proton block of L-type Ca^{2+} channels. J Gen Physiol 108:363–374

Cheng RC, Zhorov BS (2009) Docking of calcium ions in proteins with flexible side chains and deformable backbones. Eur Biophys J. E-pub Nov. 25

Cheng RC, Tikhonov DB, Zhorov BS (2009) Structural model for phenylalkylamine binding to L-type calcium channels. J Biol Chem 284:28332–28342

Corry B, Allen TW, Kuyucak S, Chung SH (2001) Mechanisms of permeation and selectivity in calcium channels. Biophys J 80:195–214

Dilmac N, Hilliard N, Hockerman GH (2003) Molecular determinants of Ca^{2+} potentiation of diltiazem block and Ca^{2+}-dependent inactivation in the pore region of cav1.2. Mol Pharmacol 64:491–501

Dilmac N, Hilliard N, Hockerman GH (2004) Molecular determinants of frequency dependence and Ca^{2+} potentiation of verapamil block in the pore region of Cav1.2. Mol Pharmacol 66:1236–1247

Doyle DA, Morais Cabral J, Pfuetzner RA, Kuo A, Gulbis JM, Cohen SL, Chait BT, MacKinnon R (1998) The structure of the potassium channel: molecular basis of K^+ conduction and selectivity. Science 280:69–77

Dudley SC Jr, Chang N, Hall J, Lipkind G, Fozzard HA, French RJ (2000) mu-conotoxin GIIIA interactions with the voltage-gated Na(+) channel predict a clockwise arrangement of the domains. J Gen Physiol 116:679–690

Ellinor PT, Yang J, Sather WA, Zhang JF, Tsien RW (1995) Ca^{2+} channel selectivity at a single locus for high-affinity Ca^{2+} interactions. Neuron 15:1121–1132

Gillespie D (2008) Energetics of divalent selectivity in a calcium channel: the ryanodine receptor case study. Biophys J 94:1169–1184

Gillespie D, Boda D (2008) The anomalous mole fraction effect in calcium channels: a measure of preferential selectivity. Biophys J 95:2658–2672

Harding MM (2001) Geometry of metal-ligand interactions in proteins. Acta Crystallogr D Biol Crystallogr 57:401–411

Harding MM (2002) Metal-ligand geometry relevant to proteins and in proteins: sodium and potassium. Acta Crystallogr D Biol Crystallogr 58:872–874

Harding MM (2004) The architecture of metal coordination groups in proteins. Acta Crystallogr D Biol Crystallogr 60:849–859

Harding MM (2006) Small revisions to predicted distances around metal sites in proteins. Acta Crystallogr D Biol Crystallogr 62:678–682

Heinemann SH, Terlau H, Stuhmer W, Imoto K, Numa S (1992) Calcium channel characteristics conferred on the sodium channel by single mutations. Nature 356:441–443

Hille B (2001) Ion channels of excitable membranes, 3rd edn. Sinauer, Sunderland

Hockerman GH, Johnson BD, Scheuer T, Catterall WA (1995) Molecular determinants of high affinity phenylalkylamine block of L-type calcium channels. J Biol Chem 270:22119–22122

Jiang Y, Lee A, Chen J, Cadene M, Chait BT, MacKinnon R (2002) Crystal structure and mechanism of a calcium-gated potassium channel. Nature 417:515–522

Jiang Y, Lee A, Chen J, Ruta V, Cadene M, Chait BT, MacKinnon R (2003) X-ray structure of a voltage-dependent K^+ channel. Nature 423:33–41

Katz AK, Glusker JP, Beebe SA, Bock CW (1996) Calcium ion coordination: a comparison with that of beryllium, magnesium, and zinc. J Am Chem Soc 118:5752–5763

Kuo CC, Hess P (1993a) Characterization of the high-affinity Ca^{2+} binding sites in the L-type Ca^{2+} channel pore in rat phaeochromocytoma cells. J Physiol 466:657–682

Kuo CC, Hess P (1993b) Ion permeation through the L-type Ca^{2+} channel in rat phaeochromocytoma cells: two sets of ion binding sites in the pore. J Physiol 466:629–655

Lazaridis T, Karplus M (1999) Effective energy function for proteins in solution. Proteins 35:133–152

Lerche C, Bruhova I, Lerche H, Steinmeyer K, Wei AD, Strutz-Seebohm N, Lang F, Busch AE, Zhorov BS, Seebohm G (2007) Chromanol 293B binding in KCNQ1 (Kv7.1) channels involves electrostatic interactions with a potassium ion in the selectivity filter. Mol Pharmacol 71:1503–1511

Li Z, Scheraga HA (1987) Monte Carlo-minimization approach to the multiple-minima problem in protein folding. Proc Natl Acad Sci U S A 84:6611–6615

Li RA, Ennis IL, French RJ, Dudley SC Jr, Tomaselli GF, Marban E (2001) Clockwise domain arrangement of the sodium channel revealed by (mu)-conotoxin (GIIIA) docking orientation. J Biol Chem 276:11072–11077

Lipkind GM, Fozzard HA (2001) Modeling of the outer vestibule and selectivity filter of the L-type Ca^{2+} channel. Biochemistry 40:6786–6794

Long SB, Campbell EB, Mackinnon R (2005) Crystal structure of a mammalian voltage-dependent Shaker family K^+ channel. Science 309:897–903

McCleskey EW (2000) Ion channel selectivity using an electric stew. Biophys J 79:1691–1692

Nonner W, Catacuzzeno L, Eisenberg B (2000) Binding and selectivity in L-type calcium channels: a mean spherical approximation. Biophys J 79:1976–1992

Parent L, Gopalakrishnan M (1995) Glutamate substitution in repeat IV alters divalent and monovalent cation permeation in the heart Ca^{2+} channel. Biophys J 69:1801–1813

Pizarro G, Fitts R, Uribe I, Rios E (1989) The voltage sensor of excitation-contraction coupling in skeletal muscle. Ion dependence and selectivity. J Gen Physiol 94:405–428

Sather WA, McCleskey EW (2003) Permeation and selectivity in calcium channels. Annu Rev Physiol 65:133–159

Talavera K, Staes M, Janssens A, Klugbauer N, Droogmans G, Hofmann F, Nilus B (2001) Aspartate residues of the Glu-Glu-Asp-Asp (EEDD) pore locus control selectivity and permeation of the T-type Ca(2+) channel alpha(1G). J Biol Chem 276:45628–45635

Tang S, Mikala G, Bahinski A, Yatani A, Varadi G, Schwartz A (1993) Molecular localization of ion selectivity sites within the pore of a human L-type cardiac calcium channel. J Biol Chem 268:13026–13029

Tikhonov DB, Zhorov BS (2005) Modeling P-loops domain of sodium channel: homology with potassium channels and interaction with ligands. Biophys J 88:184–197

Tikhonov DB, Zhorov BS (2007) Sodium channels: ionic model of slow inactivation and state-dependent drug binding. Biophys J 93:1557–1570

Tikhonov DB, Zhorov BS (2008) Molecular modeling of benzothiazepine binding in the L-type calcium channel. J Biol Chem 283:17594–17604

Tikhonov DB, Zhorov BS (2009) Structural model for dihydropyridine binding to L-type calcium channels. J Biol Chem 284:19006–19017

Weiner SJ, Kollman PA, Case DA, Singh UC, Ghio C, Alagona G, Profeta S, Weiner P (1984) A new force field for molecular mechanical simulation of nucleic acids and proteins. J Am Chem Soc 106:765–784

Weiner SJ, Kollman PA, Nguyen DT, Case DA (1986) An all atom force field for simulations of proteins and nucleic acids. J Comput Chem 7:230–252

Yang J, Ellinor PT, Sather WA, Zhang JF, Tsien RW (1993) Molecular determinants of Ca^{2+} selectivity and ion permeation in L-type Ca^{2+} channels. Nature 366:158–161

Yatani A, Bahinski A, Mikala G, Yamamoto S, Schwartz A (1994) Single amino acid substitutions within the ion permeation pathway alter single-channel conductance of the human L-type cardiac Ca^{2+} channel. Circ Res 75:315–323

Zhorov BS, Ananthanarayanan VS (1996) Structural model of a synthetic Ca^{2+} channel with bound Ca^{2+} ions and dihydropyridine ligand. Biophys J 70:22–37

Zhorov BS, Tikhonov DB (2004) Potassium, sodium, calcium and glutamate-gated channels: pore architecture and ligand action. J Neurochem 88:782–799

Zhorov BS, Folkman EV, Ananthanarayanan VS (2001) Homology model of dihydropyridine receptor: implications for L-type Ca(2+) channel modulation by agonists and antagonists. Arch Biochem Biophys 393:22–41

Zong S, Zhou J, Tanabe T (1994) Molecular determinants of calcium-dependent inactivation in cardiac L-type calcium channels. Biochem Biophys Res Commun 201:1117–1123